

Heterojuncted non-metal binary composites silicon carbide/g-C₃N₄ with enhanced photocatalytic performance

Fei Chang^{a,*}, Jiaojiao Zheng^a, Xiaofang Wang^a, Quan Xu^a, Baoqing Deng^a, Xuefeng Hu^{b,*}, Xiaoqi Liu^c

^a School of Environment and Architecture, University of Shanghai for Science and Technology, Shanghai 200093, PR China

^b Key Laboratory of Coastal Environmental Processes and Ecological Remediation, Yantai Institute of Coastal Zone Research, Chinese Academy of Sciences, Yantai, Shandong 264003, PR China

^c Institute of Tianjin Seawater Desalination and Multipurpose Utilization, State Oceanic Administration, Tianjin 300192, PR China

ARTICLE INFO

Keywords:

SiC
g-C₃N₄
Heterojunction
Photocatalysis
Active radicals
Mechanism

ABSTRACT

Novel visible-light-driven silicon carbide (SiC)/g-C₃N₄ heterojuncted composites were successfully prepared via a facile ultrasonic dispersion and calcination method, and afterwards characterized by a couple of technologies including XRD, SEM, TEM, FT-IR, XPS, UV–vis DRS, PL spectra, and N₂ adsorption-desorption. It was found that SiC nanoparticles were uniformly deposited over the surface of g-C₃N₄ to create heterojunction domains along phase interface boundary, favoring charge carriers transfer and separation across the straddling band alignments. Besides, the visible-light absorption capability of samples was enhanced by the incorporation of SiC. These physiochemical merits ensured the improved photocatalytic performance of heterojuncted composites over the degradation of dyes rhodamine B (RhB) and methyl orange (MO) in comparison to each single component SiC or g-C₃N₄. Upon an identical condition, the sample SN8 exhibited the highest photocatalytic ability among all tested samples. According to active species trapping measurements, ·OH and ·O₂[−] were deemed as major radicals and eventually a possible photocatalysis mechanism was speculated.

1. Introduction

Wastewaters containing synthetic dyes and pigments such as rhodamine B, methyl orange, and indigo carmine discharged from manufacturing inadequately addressed cause serious environmental pollution, directly affecting human health and well-being [1,2]. On account of their complicated aromatic structure and thermos-stability, most dyes are hardly decomposed by conventional physical or biochemical treatments. Instead, the photocatalytic technology, a sustainable and green route, is able to dispose of these contaminants through an oxidative degradation process. Therefore, burgeoning highly efficient visible-light-driven semiconductor-based photocatalysts becomes a matter of great urgency in the field of eliminating environmental contaminations and even converting solar energy [3,4]. A single-phased photocatalyst suffers from the fast combination of photoinduced electron-hole pairs plus relatively low photocatalytic capability, while the construction of a binary system with suitable band structures seems to be an effective manner to conquer this limitation because the charge carriers are promoted to transfer in opposite directions through a smooth phase interfaces, so as to reduce the recombination efficiently and

further promoting the photocatalytic performance [5,6]. In addition, incorporating a narrow band-gap component also conduce to the visible-light harvesting and then heighten the visible-light response of hybrid composites.

So far, the polymeric graphite-like carbon nitride (g-C₃N₄), recognized as a favorite metal-free polymeric material, has garnered particular attention in fields of water splitting for hydrogen evolving [7] and pollutant decomposition under visible light irradiation [8,9] by virtue of its appealing electronic properties as well as high thermal and chemical stability [10,11]. However, g-C₃N₄ served as a photocatalyst alone is real pinned down to its small specific surface area and severe recombination of photogenerated charge carriers [11,12]. A variety of attempts have been employed to modify g-C₃N₄, such as elements deposition [13,14], textural turning [12,15] and building a g-C₃N₄-based heterojunction with Bi₂WO₆ [16], HSbO₃ [17], BiOCl [18], WO₃ [19], Ag₃PO₄ [8], CuCr₂O₄ [20], and YVO₄ [21] etc. Specifically, Liu et al. successfully synthesized chlorine-intercalated g-C₃N₄ through a soaking-copyrolysis method [22]. Huang et al. reported the synthesis of porous g-C₃N₄ thin nanosheets by means of a template-free thiourea-assisted hydrothermal protocol [23]. Tian et al. prepared a 3D

* Corresponding authors.

E-mail addresses: feichang@usst.edu.cn (F. Chang), xfhu@yic.ac.cn (X. Liu).

mesoporous ultrathin g-C₃N₄ through a precursor-recrystallization process [24]. These modified g-C₃N₄ samples showed the significant enhancement of photo-absorption and photocatalytic degradation capabilities. Mousavi et al. constructed a series of multicomponent g-C₃N₄/Fe₃O₄/Ag₃PO₄/AgCl composites by a facile ultrasonic-irradiation method [25] and g-C₃N₄/Fe₃O₄/Ag₃PO₄/Co₃O₄ composites via ultrasonic and calcination methods as well [26]. Akhundi et al. prepared various quaternary g-C₃N₄/Fe₃O₄/AgI/Bi₂S₃ catalysts by adding different amount of Bi₂S₃ using a facile refluxing method [27] and further quaternary g-C₃N₄/Fe₃O₄/Ag/Ag₂SO₃ composites by anchoring the Ag/Ag₂SO₃ system on surface of g-C₃N₄/Fe₃O₄ in the same manner [28]. Among numerous modification strategies, the semiconductor coupling is regarded as an effective and efficacious manner to combine the advantages of intrinsic structural features from each component phase and possibly bring about a synergistic effect after hybridization [29–32].

SiC is another typical non-metallic semiconductor with an appropriate band gap of 2.3–3.3 eV [33], a more negative conduction band potential, a sufficient thermal and chemical stability, and a high mechanical strength [34], which render it extensively applied in power electronics, radio frequency devices, grinding materials [33], and to be a promising catalyst candidate under visible-light irradiation. Moreover, its high charge-carrier mobility can shuttle the photogenerated carriers swiftly before recombination from the bulk to the surface [33]. Unfortunately, the pure SiC actually exhibits a very weak photocatalytic activity, if any, from the visible to ultraviolet light as a result of the acute recombination of photogenerated charge carriers [35] and low optical response [36]. Gao et al. clearly stated the inferior photocatalytic capability of commercial α -SiC powder for water splitting under visible light in view of its small surface areas [37]. Considering the potential applications, the photocatalytic performance of SiC is generally heightened by modified its microstructure and morphology such as the morphology control [38], noble metal deposition [39], and semiconductor coupling [35,40]. Wang et al. separately deposited Pt and IrO₂ on micro-SiC surface, attaining a synergetic effect to suppressed the carriers recombination and hereby enhancing the photocatalytic activity [41]. Zou et al. attempted to decompose toluene by porous TiO₂/SiC nanocomposite films [42]. Wang et al. found that the average H₂ evolution rate increased to 4572 $\mu\text{L g}^{-1} \text{h}^{-1}$ as soon as the Pt/SiC nanowire hybrid was present [43]. If g-C₃N₄ is adopted as another ingredient to construct a composite, the well-matched band positions between SiC and g-C₃N₄ ought to kinetically facilitate the carriers transfer and separation, thereupon giving rise to the enhanced photocatalytic degradation outcome.

In this work, we attempted to construct SiC/g-C₃N₄ heterojunctioned hybrids via a simple ultrasonic dispersion and calcination route. The as-synthesized samples were systematically characterized by XRD, SEM, TEM, FT-IR, XPS, UV–vis DRS, PL spectra, and N₂ adsorption-desorption techniques. It was confirmed that SiC, a component with satisfactory visible-light absorption ability, was successfully deposited on the surface of g-C₃N₄ as irregular nanoparticles. What boosted photocatalytic efficiency over dyes degradation the produced composites take on comparing to bare SiC or g-C₃N₄ mainly owned to the favorable structural and electronic features of composites, such as strengthened light harvesting, uniform generation of heterojunction domains, and efficient separation of charge carriers along well-matched band structures. A possible photocatalysis mechanism was finally speculated based upon active radicals entrapping experiments.

2. Experiment

2.1. Materials and reagents

All chemicals of the reagent grade were utilized as received without further purifications and deionized water purified by a millipore system was used for syntheses and photocatalytic processes. Melamine, MO,

disodium ethylenediaminetetraacetate dehydrate (EDTA-2Na), terephthalic acid (TA), sodium hydroxide (NaOH), L-ascorbic acid, isopropanol alcohol (IPA), and absolute ethanol were all purchased from Sinopharm Chemical Reagent Co., Ltd. (Shanghai, China). Both SiC and RhB were provided by Shanghai Mstar Technology Ltd. and Shanghai SSS Reagent Co., Ltd. (Shanghai, China), respectively.

2.2. Samples fabrication

The pure g-C₃N₄ was produced by heating treated melamine in a semi-closed system. In a typical protocol, a desired amount of melamine with 50 mL absolute ethanol was ultrasonicated for 0.5 h and subsequently stirred for 2 h. A solid powder was segregated by filtration, dried at 60 °C for 12 h, carefully ground, charged in a semi-closed ceramic crucible, calcined in a furnace at 550 °C for 1 h with a heating rate of 10 °C min^{−1}, and finally collected as a pale-yellow powder.

As for the synthesis of SiC/g-C₃N₄ hybrid composites, a similar procedure was conducted to the above preparation except the addition of desired amount of SiC during agitation. Based upon the yield of pure g-C₃N₄ as described, changeable amounts of SiC were added and produced samples were labeled as SN0, SN1, SN5, SN8, SN20, and SN50, corresponding to the expected mass ratios of 0 (pure g-C₃N₄), 1%, 5%, 8%, 20%, and 50%, respectively. The N-TiO₂ was also constructed for comparison via a sol-gel method as previously reported [44].

2.3. Characterization

The crystal structure and surface chemical composition were analyzed by a Bruker D8 Advance X-ray diffractometer (XRD, Cu K α radiation source $\lambda = 1.05406 \text{ \AA}$) at 40 kV and 40 mA with a continuous scanning pattern in the range of 5–80° and X-ray photoelectron spectroscopy (XPS, Thermo Scientific ESCALAB 250Xi, exciting source Al K α radiation, $h\nu = 1486.8 \text{ eV}$). The C1s band was set on 284.6 eV as a reference to calibrate other binding energies. A scanning electron microscopy (SEM, QUANTA F250) and transmission electron microscopy (TEM, Tecnai G2 F20) were employed to measure the morphological and microstructural properties. The UV–vis diffuse reflectance spectra (UV–vis DRS) were analyzed on a spectrophotometer (Shimadzu UV2600, Japan) ranging from 200 to 800 nm for detecting optical features of samples and the BaSO₄ was used as a reflectance standard. Fourier-transform infrared (FT-IR) spectra were taken on a Bruker V-70 Fourier transform-infrared spectrophotometer in the frequency range of 500–4000 cm^{−1}. Photoluminescence (PL) spectra were recorded on an Edinburgh FLSP920 fluorescence spectrometer. N₂ adsorption-desorption isotherms were evaluated on a Micromeritics ASAP2020HD88 system at 77 K and the pore size distribution was calculated by the Barrett-Joyner-Halenda (BJH) method. All samples were degassed at 120 °C for 4 h prior to measurements.

2.4. Photocatalytic activity evaluations

The photocatalytic behavior of as-prepared samples was checked over the degradation of dye RhB and MO in a photocatalytic reactor. A 300 W Xenon lamp (CEL-HXF300, AuLight, Beijing) was served as a visible light source with a 420–780 nm cut-off filter fixed to assure the presence of only visible light. The reactor stayed in a water channel with a continuous circulation of cold water to maintain a constant temperature and the light source was 20 cm away from the surface of aqueous suspension. The photocatalyst (20 mg) was immersed in an aqueous solution of RhB (20 mg L^{−1}, 80 mL) or MO (5 mg L^{−1}, 80 mL) under a continuous stir. Prior to the visible-light illumination, the suspension was strongly magnetically stirred in dark for 1 h to reach an adsorption-desorption balance between organic molecules and catalysts surface. During irradiation, 3 mL aliquot was taken from the suspension at every 30 min intervals and separated by centrifugation twice. The residue concentrations of RhB and MO were estimated on a UV–vis

spectrophotometer (Purkinje General T6) through the measurement of the absorbance at 554 nm and 463 nm, respectively.

2.5. Active species capture experiments

Reagents IPA, L-ascorbic acid, or EDTA-2Na was released into the reaction mixture to enrapture active species such as hydroxyl radicals ($\cdot\text{OH}$), superoxide radicals ($\cdot\text{O}_2^-$), or produced holes (h^+), respectively. The procedure was similar to the photocatalytic capability test except that the capture reagent was added with a concentration of 5 mM. Since the TA could convert to a highly fluorescent 2-hydroxyterephthalic acid after reacting with generated $\cdot\text{OH}$ radicals, it is feasible to use TA (0.5 mM in a 2 mM NaOH aqueous solution) as a probe molecule to detect the amount of $\cdot\text{OH}$ radicals during photocatalytic process in the presence of sample SN8 at an excitation wavelength of 324 nm in PL emission spectrometer. The procedure was almost as the same as the one described above except the addition of TA instead of RhB.

3. Results and discussion

3.1. XRD patterns

XRD patterns of SiC/ $g\text{-C}_3\text{N}_4$ hybrid series with different mass ratios, pure SiC, and $g\text{-C}_3\text{N}_4$ are shown in Fig. 1. The characteristic diffraction peaks of pure $g\text{-C}_3\text{N}_4$ are in good agreement with the tetragonal phase $g\text{-C}_3\text{N}_4$ (JCPDS 87-1526) and both intensive peaks at 13.0° and 27.4° can be indexed to (100) and (002) diffraction planes, assigning to the in-plane structure stacking motif of tri-s-triazine units and the inter-layer packing reflection of aromatic moieties, respectively [16,24]. Diffraction peaks centered at 35.7° , 41.4° , 60.1° , and 71.9° are relevant to the (111), (200), (220), and (311) crystallographic planes of cubic phase SiC (JCPDS 29-1129). A weak peak at 33.7° originates from a spontaneous packing fault accompanying with the growth of SiC [45]. As to SN composite series, all diffraction peaks belonging to $g\text{-C}_3\text{N}_4$ phase become weakened by degrees in pace with the enrichment of SiC content from 1% to 50% and on the contrary, feature peaks ascribing to the SiC phase become gradually strengthened, revealing the high dispersion of SiC nanoparticles over the $g\text{-C}_3\text{N}_4$ surface. In addition, diffraction peaks corresponding to other substances or impurities can be unobserved in these composites, certifying the high purity of those as-prepared samples.

3.2. SEM and TEM images

The surface morphology of as-prepared samples was visualized by SEM images. As depicted in Fig. 2A, the pure $g\text{-C}_3\text{N}_4$ prepared by the calcination of melamine displays numerous irregular large aggregates

comprising lamellar structures. By contrast, a large number of irregular nanoparticles with the size around 60 nm are observed in the pure commercial SiC in Fig. 2B. As found in SN hybrids images shown in Figs. 2C–F, some irregularly-shaped SiC nanoparticles remarked with red arrows are uniformly deposited on the surface of $g\text{-C}_3\text{N}_4$ large aggregates and the number of SiC nanoparticles raises with the augmentation of SiC contents. Particularly, the accumulation of the small SiC nanoparticles induces the almost coverage of the entire surface of $g\text{-C}_3\text{N}_4$ large aggregates in sample SN50 according to Fig. 2F. The even deposition of SiC nanoparticles on surface of $g\text{-C}_3\text{N}_4$ in SEM images is responsible for the reinforcement of SiC diffraction peaks and the abatement of $g\text{-C}_3\text{N}_4$ diffraction peaks in XRD patterns.

TEM images were recorded to further investigate the morphology and microstructure of the pure $g\text{-C}_3\text{N}_4$ and composite SN8. As exhibited in Fig. 3A, the individual $g\text{-C}_3\text{N}_4$ is composed of lamellar nanosheet structures with some wrinkles at the edge. Notably, some pore-like domains can be easily found, which could be attributed to the slowly releasing of ammonia or other gaseous materials during the samples synthetic process at a high calcination temperature [46]. For the composite SN8 in Fig. 3B, the original lamellar structure of $g\text{-C}_3\text{N}_4$ is still remained with the presence of some small SiC nanoparticles clearly found on the boundary, remarked by a red dotted elliptical frame. These particles in TEM image is relatively small in size in comparison to those in SEM images, possibly attributing to the ultrasonic treatment prior to the TEM analysis.

3.3. FT-IR spectra

FT-IR spectra of pure SiC, $g\text{-C}_3\text{N}_4$, and SN hybrids were recorded to check surface chemical groups and bonding, as depicted in Fig. 4. The spectrum of pure $g\text{-C}_3\text{N}_4$, denoted as SN0, shows three typical absorption regions around 810, 1250–1650, and 3000–3600 cm^{-1} . The broad absorption band ranging from 3000 to 3600 cm^{-1} is assigned to the stretching and bending vibrations of residual N-H or adsorbed O-H groups [47], while the peak at 1250–1650 cm^{-1} is relevant to the typical stretching vibration of CN heterocycles and the sharp peak centered at 810 cm^{-1} represents the characteristic breathing mode of triazine units [30]. As to the spectrum of pure SiC, an intensive absorption band at 858 cm^{-1} can be ascribed to the Si-C stretching vibration modes [48], and both peaks at 470 cm^{-1} and 1090 cm^{-1} are indexed to the Si-O stretching vibrations, mainly caused by the slight oxidation of SiC surface [34,49]. With regard to SiC/ $g\text{-C}_3\text{N}_4$ composites, the feature absorption peaks of $g\text{-C}_3\text{N}_4$ are well maintained, while the sharp peak positioned around 858 cm^{-1} , marked by a red square frame and its enlarged image placed on the right, is gradually widened with the increase of SiC contents to become a bump that is characteristic vibration of Si-C bonds, evidently signifying the coexistence of both components.

3.4. XPS analysis

XPS analysis was conducted to further explicate surface chemical compositions and elemental valence state in the as-prepared hybrid SN8, as seen in Fig. 5. The full scan XPS spectrum in Fig. 5A indicates the presence of Si, C, and N elements in sample SN8, confirming the coexistence of both ingredients of $g\text{-C}_3\text{N}_4$ and SiC. In addition, the element O is also detected and possibly originates from oxygen-containing species adsorbed or slight oxidation of Si species on surface. The high-resolution XPS spectra of C 1s in Fig. 5B contains three peaks with binding energies at 284.6 eV, 287.8 eV, and 288.3 eV, respectively indexing to the C-C bonds of adventitious external carbon [24], the defect-containing sp^3 -coordinated carbon atoms on $g\text{-C}_3\text{N}_4$ surface [50], and the sp^2 -hybridized carbons in the aromatic rings (N-C=N), revealing the existence of $g\text{-C}_3\text{N}_4$ phase [50]. The N 1s spectrum in Fig. 5C was deconvoluted into three component peaks centered at 398.3 eV, 399.7 eV, and 400.6 eV. The main N 1s peak at 398.3 eV

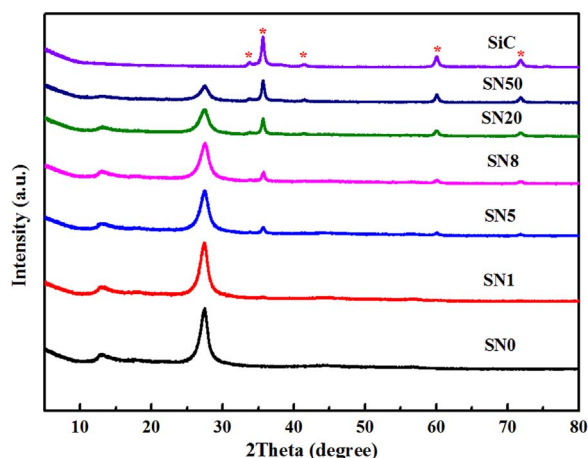


Fig. 1. XRD patterns of bare SiC, $g\text{-C}_3\text{N}_4$, and SNx hybrid composites.

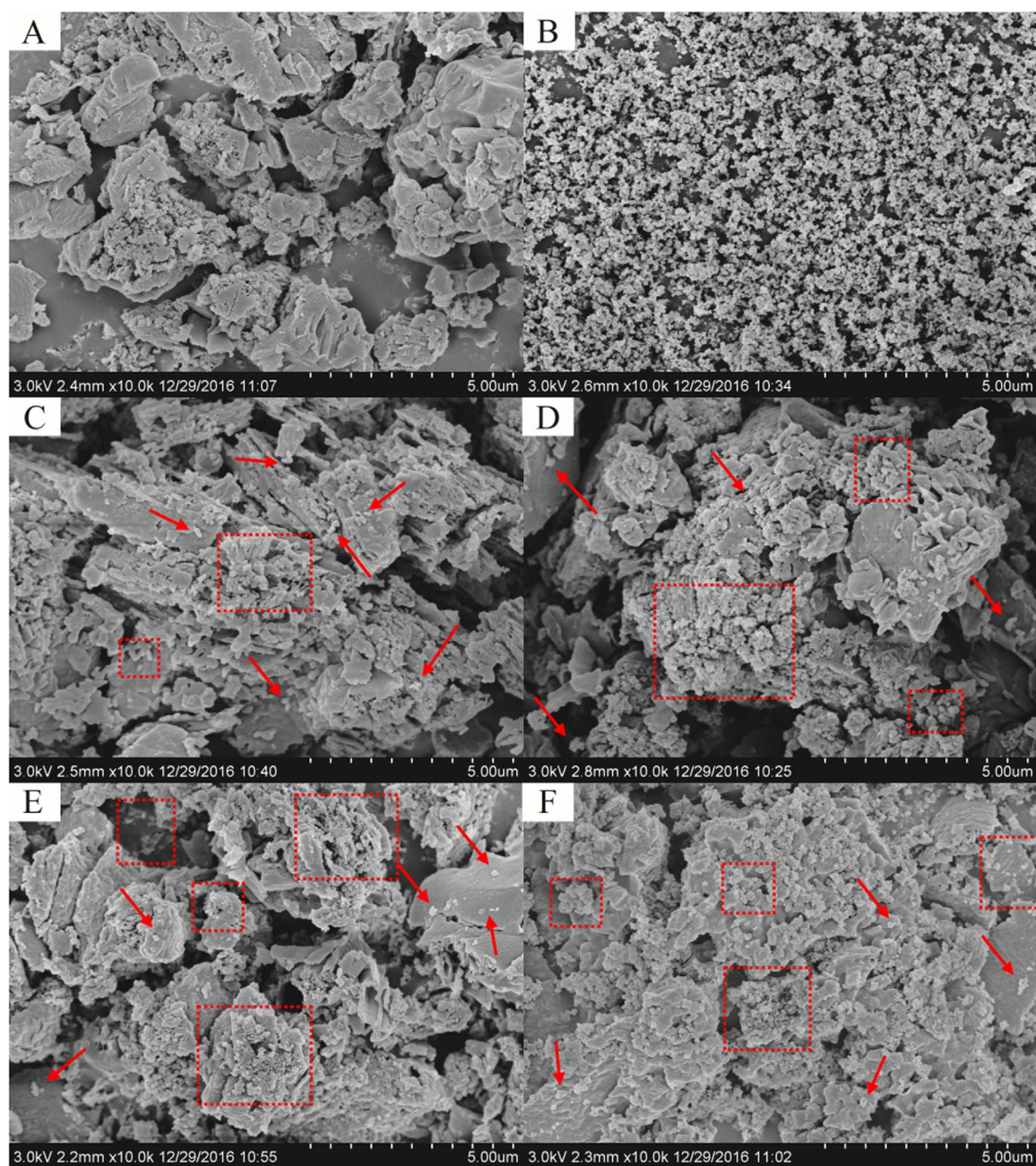


Fig. 2. SEM images of samples (A) SN0, (B) SiC, (C) SN1, (D) SN8, (E) SN20, and (F) SN50.

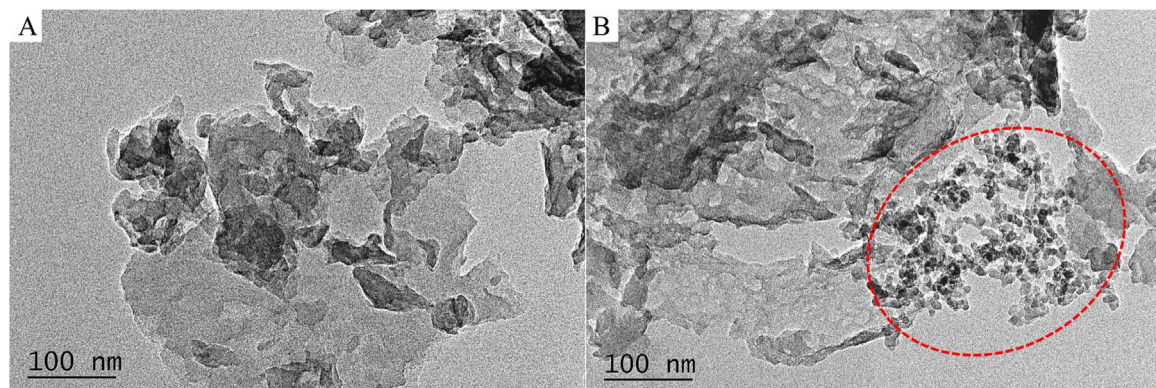


Fig. 3. TEM images of samples (A) SN0 and (B) SN8.

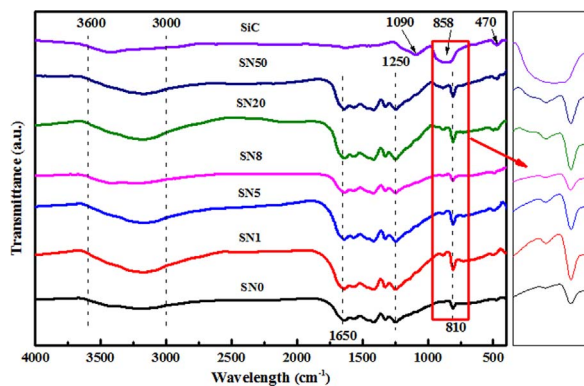


Fig. 4. FT-IR spectra of bare SiC, g-C₃N₄, and SN_x hybrid composites.

corresponds to sp²-hybridized nitrogen in triazine rings (C=N-C) [51]. Another peak at 399.7 eV was assigned to the bringing N bonded to the tertiary N in N-(C)₃ [52], and a weak peak located at 400.6 eV was identified as amino groups carrying hydrogen (-NHx) [16]. As for Si 2p spectrum in Fig. 5D, both peaks at 100.5 eV and 102.6 eV are attributed to the Si-C and Si-O bonds [43], respectively, which is in good accordance with the result of FT-IR analysis.

3.5. UV-vis DRS spectra

The optical property and band gap feature of as-prepared samples were examined by UV-vis diffuse reflectance spectra in Fig. 6A. Pure SiC with a color of deep green shows a strong absorption from the ultraviolet to visible light region and thus can be a suitable component to

construct an efficient hybrid system with g-C₃N₄ that presents an absorption edge at about 480 nm. For SN composites, the absorption intensities ranging from 420 nm to 800 nm was gradually strengthened and the absorption edges are markedly shifted to the long wavelength, namely bathochromic shift, with the increase of SiC addition, revealing the enhancement of visible-light harvesting and also an evidence of good interaction between both components in the hybrid system [32]. The band gap energy (E_g) of pure SiC and g-C₃N₄ is able to be estimated according to the following formula:

$$ah\nu = A(h\nu - E_g)^{2/n}$$

where a , h , ν and A are absorption coefficient, plank constant, light frequency, and a constant, respectively [5,19]. The value n above depends on the characteristic of optical transition in a semiconductor ($n = 1$ for the direct transition and $n = 4$ for the indirect transition) [18], which can be deduced by plotting $\ln(ah\nu)$ versus $\ln(h\nu - E_g)$ to form a straight line and the corresponding slope is the hinge because the material belongs to an indirect or direct transition semiconductor when the slope equals or unequals to 1, respectively. From the Fig. 6B, the slopes of both pure SiC and g-C₃N₄ are determined as 0.89 and 0.12, indicating that both original ingredients undergo a direct transition, that is, the value n as 1. Accordingly, the E_g values of pure SiC and g-C₃N₄ were calculated to be 2.57 eV and 2.48 eV, respectively, determined from the intercept of the tangential line of $(ah\nu)^{1/2}$ vs $h\nu$. It is general that the band edge potentials of VB and CB of pure SiC and g-C₃N₄ can be calculated using both empirical equations as below [6]:

$$E_{VB} = X - E^e + 0.5E_g$$

$$E_{CB} = E_{VB} - E_g$$

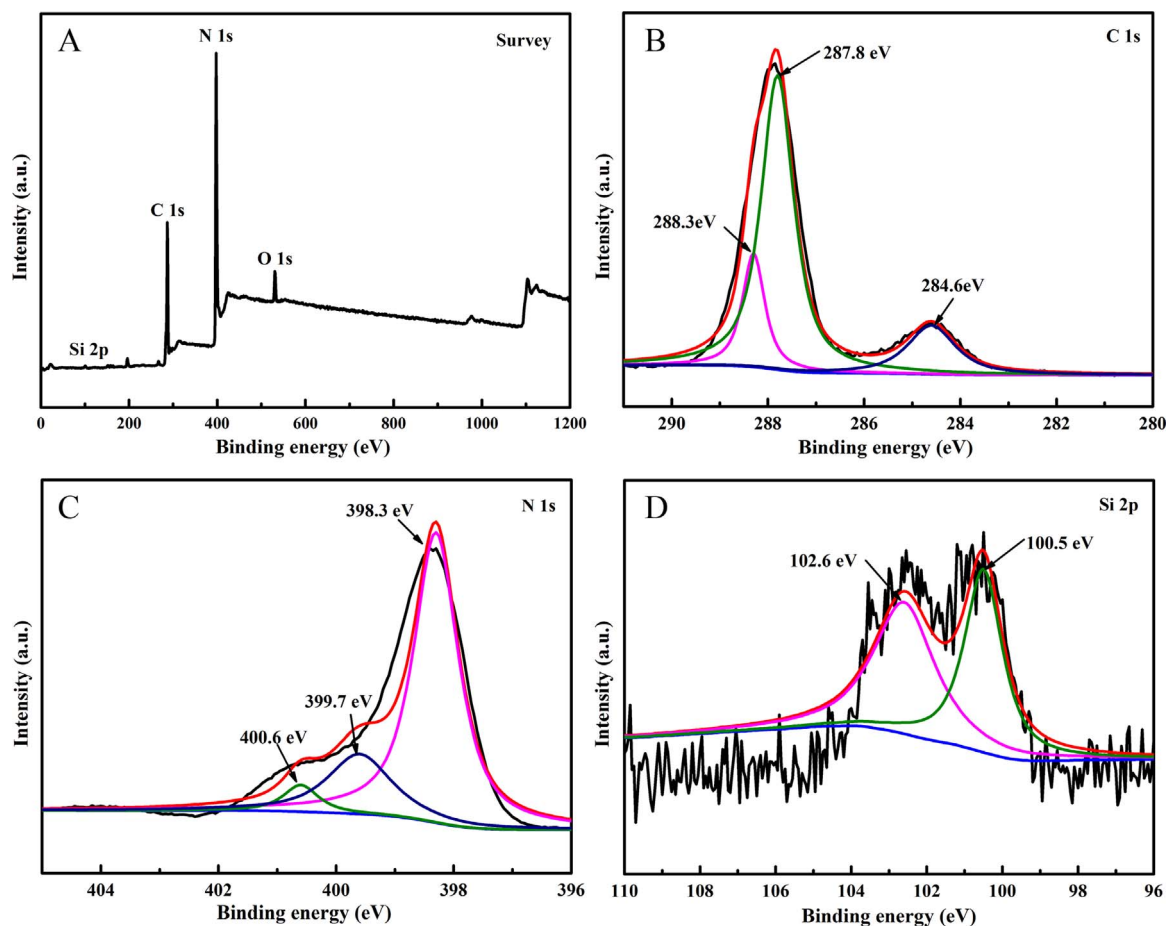


Fig. 5. XPS survey spectrum (A) and corresponding high-resolution XPS spectra: C 1s (B), N 1s (C), and Si 2p (D) of sample SN8.

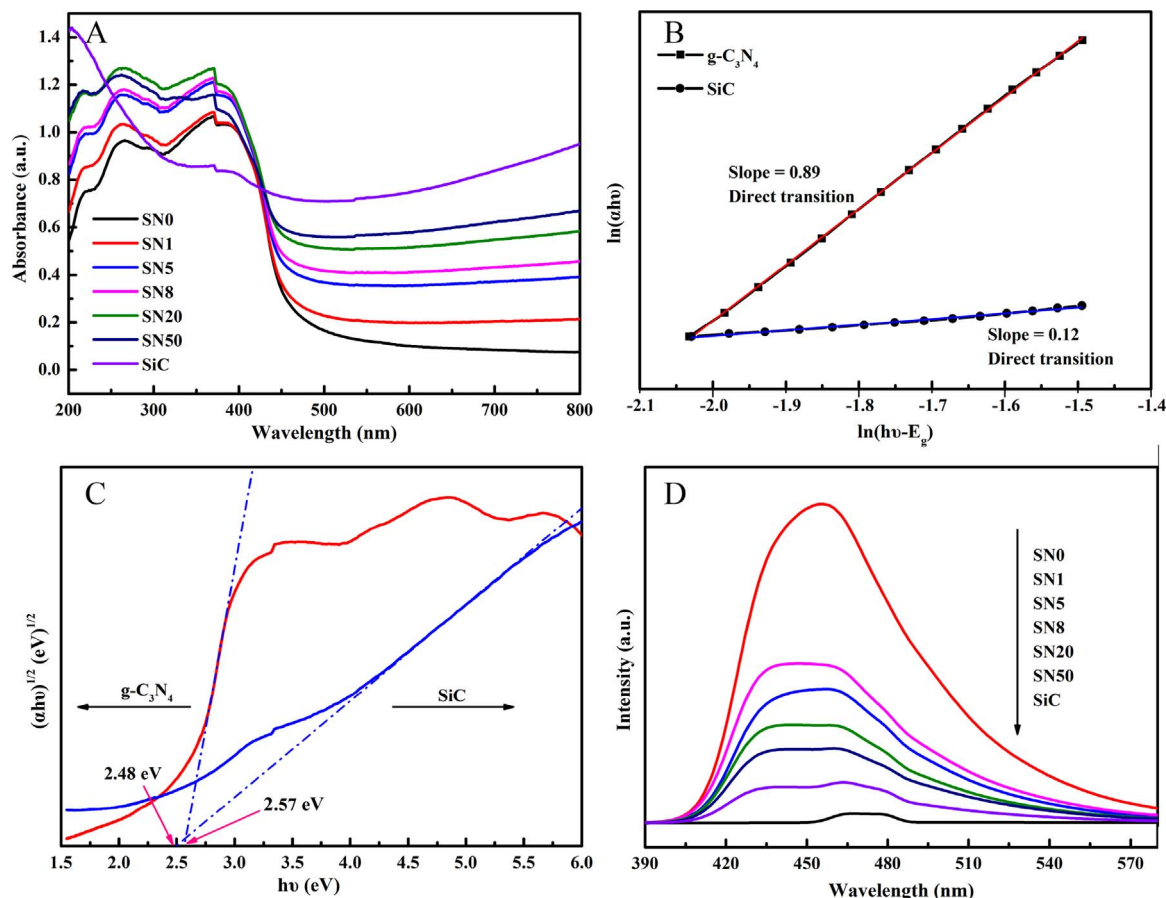


Fig. 6. UV-vis DRS spectra of as-prepared samples (A), $\ln(\alpha h\nu)$ vs $\ln(h\nu-E_g)$ (B), E_g values of samples SiC and SN0 (C), and PL spectra of as-prepared samples.

where E_{VB} , E_{CB} , X , and E° are defined as the valence band (VB) and conduction band (CB) edge potentials, the Mulliken's electronegativity, and the energy of free electrons on the hydrogen scale (~ 4.5 eV), respectively [18]. The X values for SiC and $g-C_3N_4$ are defined as 5.47 eV and 4.73 eV [6], respectively. Consequently, the VB and CB potentials of SiC and $g-C_3N_4$ can be estimated to be 2.21 eV and -0.27 eV, 1.52 eV and -1.05 eV, respectively. Apparently, both semiconductors SiC and $g-C_3N_4$ with well-matched electronic structures are beneficial to create heterojunction that ensure the efficient transfer and separation of photoinduced charge carriers and further advance photocatalytic performance.

3.6. PL

The PL spectra were measured to elucidate the transfer and separation efficiency of photogenerated charge carriers in as-prepared samples [5,53]. Generally, a relatively weak PL band means the low recombination rate in semiconductors [24]. Obviously, in Fig. 6D, the pure $g-C_3N_4$ shows a strong and wide emission band in the wavelength range of 400–600 nm, implying the high recombination of photo-produced electron-hole pairs. By comparison, the pure SiC exhibits a quite weak PL emission band. The SN series present band curves possessing both band features of these two components and moreover, the intensity of these curves reduces gradually accompanying the increase of SiC contents, suggesting the efficient charge carriers separation

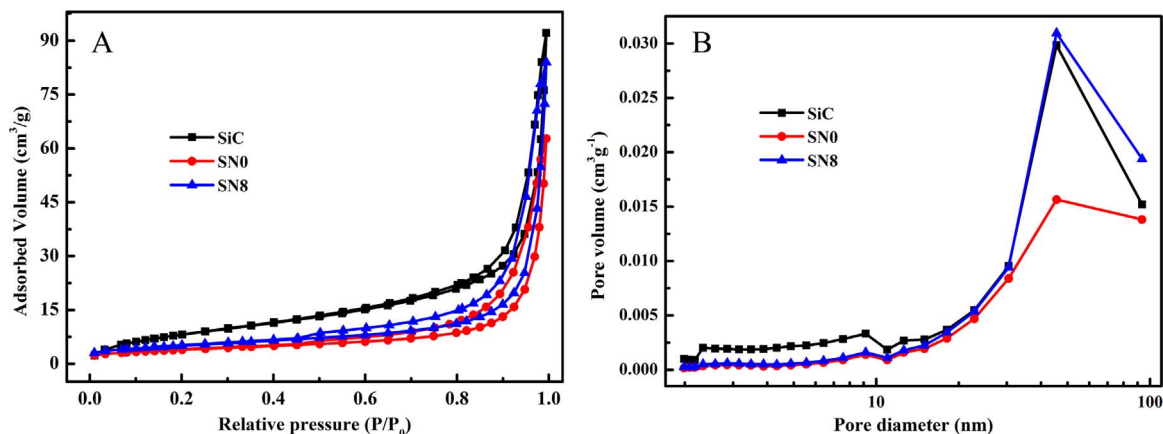


Fig. 7. Nitrogen adsorption-desorption isotherms (A) and corresponding pore size distribution curves of SiC, SN0 and SN8 (B).

Table 1
Textural properties of all as-synthesized composites and SiC.

Samples	S_{BET} ($\text{m}^2 \text{g}^{-1}$)	Average pore size (nm)	Pore volume ($\times 10^{-2} \text{cm}^3 \text{g}^{-1}$)
SiC	46.1	7.84	9.02
SN0	13.2	13.4	4.61
SN1	12.9	13.6	4.14
SN5	16.8	15.8	6.61
SN8	17.9	15.4	6.68
SN20	20.1	15.6	7.82
SN50	22.2	13.9	7.76

caused by the formation of heterostructures.

3.7. N_2 adsorption-desorption isotherms

Fig. 7 displays the N_2 adsorption-desorption isotherms and the corresponding pore size distribution curves of samples SiC, SN0 and SN8. The adsorption-desorption isotherms of all samples in Fig. 7A can be classified as the typical type IV pattern with a H_3 -type hysteresis loop based on the IUPAC classification, suggesting the formation of slit-like mesopores. Besides, the adsorption branches of these samples gradually and continuously increase along with the increase of relative pressures approaching to 1, which is quite similar to the type II isotherm and indicates the presence of macropores [48]. The appearances of both mesopores and macropores are confirmed in Fig. 7B, which are resulted from the aggregation of plate-like particles and bulky clusters, respectively. In addition, the specific surface areas (S_{BET}) of all samples were collected and summarized in Table 1. Compared with that of SN0, S_{BET} values of binary composites are slightly enlarged with the enhancement of SiC contents, quite similar to the variation of average pore size and pore volumes. The slightly increased S_{BET} and pore volumes are able to expose more active sites to contaminant molecules, thus benefiting their photocatalytic performance.

3.8. Photocatalytic degradation performance

The photocatalytic performance of as-synthesized samples was mensurated at room temperature by the degradation of RhB and MO under visible-light irradiation. Adsorption-desorption equilibria were achieved for all photocatalytic tests through a magnetic stir for 1 h in dark before exposing to the illumination. As depicted in Fig. 8A, the photolysis of RhB, a blank experiment without any catalysts, was carried out and can be negligible, demonstrating the sufficient photo and chemical stability of RhB. Both N-TiO_2 and SiC are of poor photocatalytic capabilities over RhB, providing degradation efficiencies of 15% and 11% after 150 min visible-light irradiation, respectively. Pure $\text{g-C}_3\text{N}_4$ exhibits a relatively low photocatalytic performance that can be enhanced by the formation of binary composites with another component SiC. Exactly as the results display, with the increase of SiC contents in SN composites, the photocatalytic outcome can be improved and then decreased beyond mass ratio of 8%. Consequently, the sample SN8 possesses the best photocatalytic degradation ability among all tested samples. The photocatalytic degradation reaction is in accordance with the pseudo-first-order kinetics and the corresponding apparent rate constant (k) can be deduced by the following equation:

$$\ln(C_0/C) = kt$$

where C_0 and C are measured concentrations of RhB at the illumination time (t) of $t = 0$ and t [21]. Apparently, the sample SN8 in Fig. 8B manifests the highest apparent rate constant 0.00619 min^{-1} that is 30.9 times, 1.2 times, and 5.2 times of those SiC, $\text{g-C}_3\text{N}_4$, and N-TiO_2 , respectively.

Meanwhile, MO was also chosen as a representative model pollutant to evaluate the photocatalytic performance of as-obtained samples

under the identical experimental condition, as shown in Fig. 8C. It has been found that either photolysis or degradation of MO molecules using SiC as a catalyst is ignorable. Both samples SN0 and N-TiO_2 are able to exert photocatalytic decompositions with enhanced efficiencies that can be further improved when composite SN8 is utilized. Correspondingly, the composite SN8 presents an apparent rate constant that is almost 6.7 times and 1.6 times as high as that of pure SiC and $\text{g-C}_3\text{N}_4$ samples in Fig. 8D.

During above photocatalytic processes, composites SN, particularly the sample SN8, exhibit enhanced degradation efficiencies in comparison to bare SiC and $\text{g-C}_3\text{N}_4$, which can possibly own to those reasons described below. Firstly, the visible-light absorption and utilization of SN composites are greatly strengthened since the bare SiC is strongly responsive to the visible light, as discussed in UV-vis DRS spectra. Secondly, well-matched band structures of both components tend to generate the straddling band alignments along the heterostructure edge that promote the transfer and separation of charge carriers effectively, favoring the best use of electrons and holes for degradation reactions. Thirdly, as to SN composites, the increase of SiC content facilitates the visible-light harvesting and beyond the optimal SiC content of 8%, an excess amount of SiC tends to cover the whole surface of $\text{g-C}_3\text{N}_4$ and further impeded the excitation of $\text{g-C}_3\text{N}_4$. Therefore, composites SN with suitable physicochemical merits are able to trigger photocatalytic processes with satisfactory decomposition efficiencies.

3.9. Photocatalysis mechanism inspected

Reactive radical species such as $\cdot\text{OH}$, $\cdot\text{O}_2^-$, and holes possibly involved in the photocatalytic degradation processes were detected by adding some scavenger reagents in the presence of sample SN8 for the sake of the photocatalysis mechanism inspection [54]. Specifically, both reagents EDTA-2Na and IPA were added to respectively trap radical species h^+ and $\cdot\text{OH}$ [19,51]. Photoproduced radicals $\cdot\text{O}_2^-$ was ensnared by the introduction of L-ascorbic acid instead of *p*-benzoquinone since the latter was not quite stable in some photocatalytic processes [54]. In addition, the O_2 isolation experiment was performed by bubbling N_2 to further confirm the generation of radicals $\cdot\text{O}_2^-$. As shown in Fig. 9A, the addition of reagent EDTA-2Na exerts almost no influence on the photocatalytic degradation of RhB molecules, while the presence of L-ascorbic acid greatly inhibited the removal efficiency. The crucial role of radicals $\cdot\text{O}_2^-$ is also confirmed by the introduction of N_2 gas to expel dissolved O_2 molecules that readily convert to $\cdot\text{O}_2^-$ species via a one-electron reduction path [8]. In addition, the photocatalytic degradation is somewhat restrained as soon as reagent IPA is involved, implying the minor effect of radicals $\cdot\text{OH}$ on photocatalytic processes.

The generation of radicals $\cdot\text{OH}$ was also detected through the addition of TA in Fig. 9B since TA reacts with $\cdot\text{OH}$ to generate a fluorescent product 2-hydroxy terephthalic acid at 425 nm [30,55]. It is clear that the intensity of fluorescent band in the wavelength range from 380 to 550 nm gradually increased with the extension of irradiation time, suggesting the indeed presence of oxidative radicals $\cdot\text{OH}$ in the reaction system.

According to band structures of both SiC and $\text{g-C}_3\text{N}_4$ components and active species trapping experiments, a primary photocatalytic mechanism is proposed to demonstrate the transfer and separation of electron-hole pairs and further degradation reactions, as exhibited in Fig. 10. Upon a visible-light irradiation, both semiconductors SiC and $\text{g-C}_3\text{N}_4$ are prone to excite and thus electrons and holes are produced at CB and VB. Because of the internal static electric field, electrons tend to transfer from the CB of $\text{g-C}_3\text{N}_4$ to that of SiC and holes migrate from the VB of SiC to that of $\text{g-C}_3\text{N}_4$. Therefore, electrons and holes are distributed in different components caused by the well-aligned band structures in composites. Electrons gathered at the CB of SiC react with surface-adsorbed oxygen molecules to produce radicals $\cdot\text{O}_2^-$ as the CB level (-0.27 eV) is more negative than that of $\text{O}_2/\cdot\text{O}_2^-$ (-0.046 eV) [56]. Meanwhile, holes collected at the VB of $\text{g-C}_3\text{N}_4$ are insufficient to

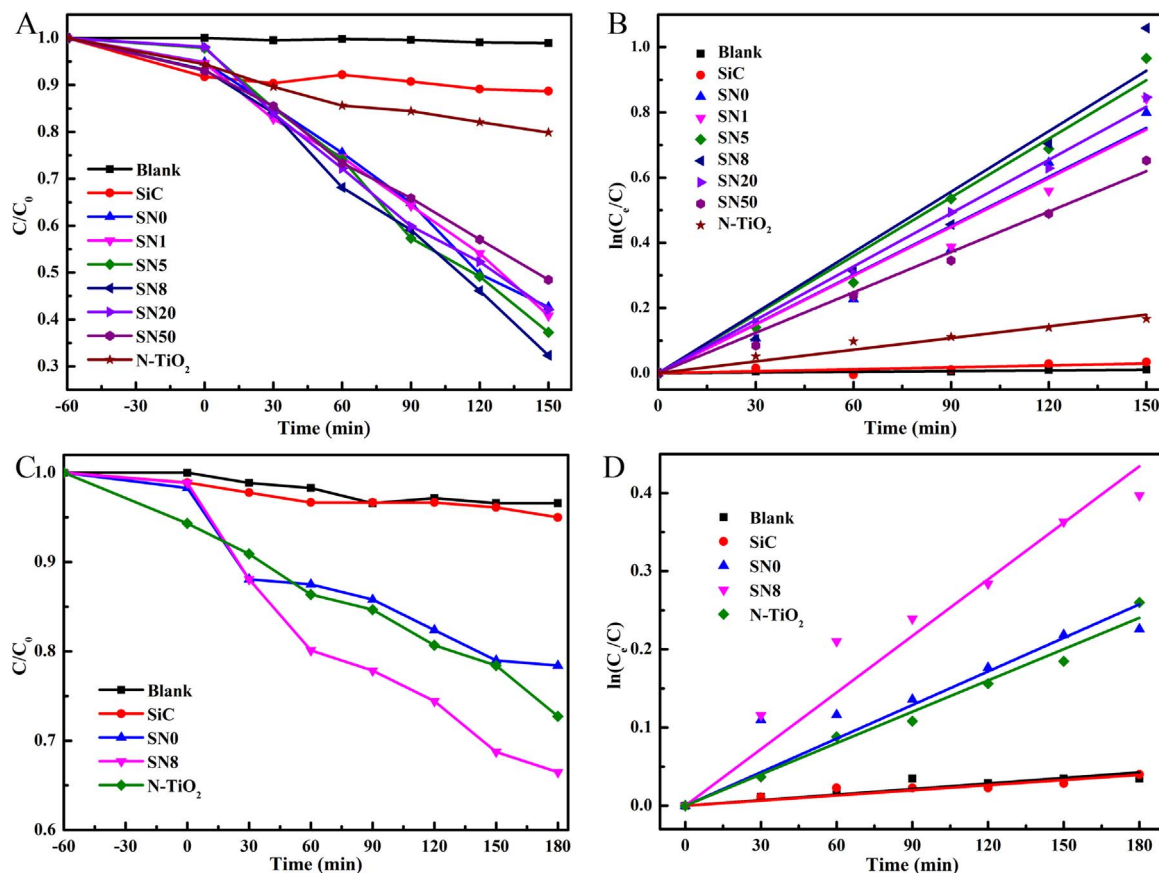


Fig. 8. Photocatalytic degradation of RhB over series of as-prepared samples (A), the corresponding variation of apparent rate constants (B), photocatalytic degradation of MO (C), the corresponding variation of apparent rate constants (D).

react with OH^- or H_2O species to generate radicals $\cdot\text{OH}$ since the VB level of $\text{g-C}_3\text{N}_4$ (1.52 eV) is more negative than $\text{E}^\circ(\text{H}_2\text{O}/\cdot\text{OH} = +2.38 \text{ eV})$ [18], even $\text{E}^\circ(\text{OH}^-/\cdot\text{OH} = +1.99 \text{ eV})$ [57]. As a result, it is deduced that radicals $\cdot\text{OH}$ may possibly generate via a two-electron oxidation pathway. As a result, the redistribution of electrons and holes and a series of subsequent reactions accelerate the separation of charge carriers and prolong the lifetime of charge carriers, thus boosting the photocatalytic degradation performance of SN composites.

4. Conclusions

In summary, a series of binary composites were successfully fabricated and further characterized through a collection of analytical

techniques. SEM images depicted that SiC nanoparticles evenly deposited on the surface of $\text{g-C}_3\text{N}_4$ sheets and TEM images confirmed the presence of heterojunction domains at the edge of phase boundary. Meanwhile, UV-vis DRS spectra demonstrated an obviously enhanced visible light harvesting compared to pure $\text{g-C}_3\text{N}_4$. The improved photocatalytic capability of these hybrid composites, especially the sample SN8, under visible-light irradiation might be caused by a synergistic effect, including the suitable morphology, strengthened visible-light harvesting, and well-aligned straddling band structures. A possible photocatalytic mechanism was eventually proposed according to the active species trapping experiments and band structures of both semiconductor components.

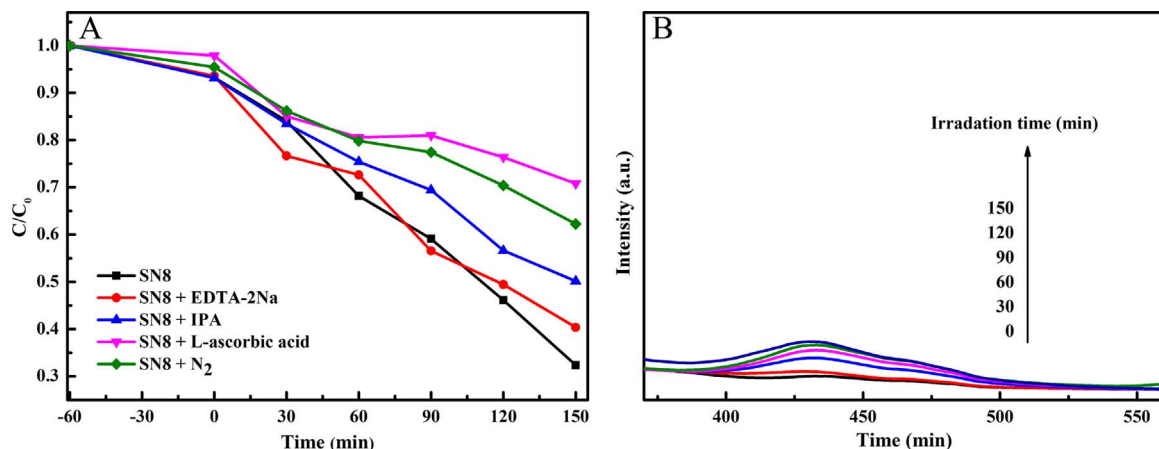


Fig. 9. Active species trapping experiments using sample SN8 (A) and hydroxyl radicals quantification experiments of sample SN8.

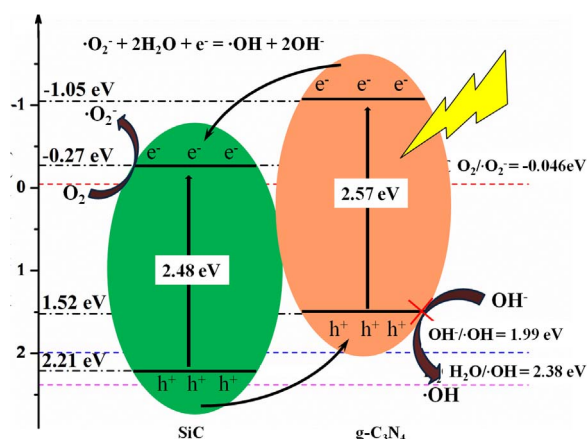


Fig. 10. A proposed photocatalysis mechanism of binary composites under visible-light irradiation.

Acknowledgements

The study was financially supported by the National Natural Science Foundation of China (No. 21207089), the Natural Science Foundation of Shanghai (No. 17ZR1419200), the project-sponsored by SRF for ROCS, SEM., and the science and technology development project of University of Shanghai for Science and Technology (2017KJFZ073).

References

- [1] X. Wang, J. Wang, P. Guo, W. Guo, C. Wang, Degradation of rhodamine B in aqueous solution by using swirling jet-induced cavitation combined with H_2O_2 , *J. Hazard. Mater.* 169 (2009) 486–491.
- [2] B.H. Hameed, Spent tea leaves: a new non-conventional and low-cost adsorbent for removal of basic dye from aqueous solutions, *J. Hazard. Mater.* 161 (2009) 753–759.
- [3] L.Y. Chen, W.D. Zhang, $\text{In}_2\text{O}_3/\text{g-C}_3\text{N}_4$ composite photocatalysts with enhanced visible light driven activity, *Appl. Surf. Sci.* 301 (2014) 428–435.
- [4] J. Di, J. Xia, S. Yin, H. Xu, M. He, $\text{Ag-C}_3\text{N}_4/\text{BiOBr}$ visible-light-driven composite: synthesis via a reactable ionic liquid and improved photocatalytic activity, *RSC Adv.* 3 (2013) 19624–19631.
- [5] S. Chen, Y. Hu, X. Jiang, S. Meng, X. Fu, Fabrication and characterization of novel Z-scheme photocatalyst $\text{WO}_3/\text{g-C}_3\text{N}_4$ with high efficient visible light photocatalytic activity, *Mater. Chem. Phys.* 149–150 (2015) 512–521.
- [6] S.F. Chen, Y.F. Hu, S.G. Meng, Study on the separation mechanisms of photo-generated electrons and holes for composite photocatalysts $\text{g-C}_3\text{N}_4\text{-WO}_3$, *Appl. Catal. B: Environ.* 150–151 (2014) 564–573.
- [7] X.J. Zou, Y.Y. Dong, X.Y. Li, Q.D. Zhao, Y.B. Cui, G. Lu, Inorganic–organic photocatalyst $\text{BiPO}_4/\text{g-C}_3\text{N}_4$ for efficient removal of gaseous toluene under visible light irradiation, *Catal. Commun.* 69 (2015) 109–113.
- [8] S. Kumar, T. Surendar, A. Baruah, Synthesis of a novel and stable $\text{g-C}_3\text{N}_4\text{-Ag}_3\text{PO}_4$ hybrid nanocomposite photocatalyst and study of the photocatalytic activity under visible light irradiation, *J. Mater. Chem. A* 1 (2013) 5333–5340.
- [9] H.H. Ji, F. Chang, X.F. Hu, W. Qin, J.W. Shen, Photocatalytic degradation of 2,4,6-trichlorophenol over $\text{g-C}_3\text{N}_4$ under visible light irradiation, *Chem. Eng. J.* 218 (2013) 183–190.
- [10] H.P. Li, J.Y. Liu, W.G. Hou, Synthesis and characterization of $\text{g-C}_3\text{N}_4/\text{Bi}_2\text{MoO}_6$ heterojunctions with enhanced visible light photocatalytic activity, *Appl. Catal. B: Environ.* 160–161 (2014) 89–97.
- [11] Y. Li, Y. Sun, D. Dong, W.K. Ho, Enhancing the photocatalytic activity of bulk $\text{g-C}_3\text{N}_4$ by introducing mesoporous structure and hybridizing with graphene, *J. Colloid Interface Sci.* 436 (2014) 29–36.
- [12] F. Dong, Y. Li, Z. Wang, W.K. Ho, Enhanced visible light photocatalytic activity and oxidation ability of porous graphene-like $\text{g-C}_3\text{N}_4$ nanosheets via thermal exfoliation, *Appl. Surf. Sci.* 358 (2015) 393–403.
- [13] S.W. Cao, Y.P. Yuan, B. James, S.C.J. Loo, X. Can, Noble-metal-free $\text{g-C}_3\text{N}_4/\text{Ni}(\text{dmgH})_2$ composite for efficient photocatalytic hydrogen evolution under visible light irradiation, *Appl. Surf. Sci.* 319 (2014) 344–349.
- [14] F. Dong, Z. Zhao, Y. Sun, Y. Zhang, S. Yan, An advanced semimetal-organic Bi spheres- $\text{g-C}_3\text{N}_4$ nanohybrid with SPR-enhanced visible-light photocatalytic performance for NO purification, *Environ. Sci. Technol.* 49 (2015) 12432–12440.
- [15] X. Wang, S. Blechert, M. Antonietti, Polymeric graphitic carbon nitride for heterogeneous photocatalysis, *ACS Catal.* 2 (2012) 1596–1606.
- [16] Y.L. Tian, B.B. Chang, J.L. Lu, J. Fu, F.N. Xi, X.P. Dong, Hydrothermal synthesis of graphitic carbon nitride- Bi_2WO_6 heterojunctions with enhanced visible light photocatalytic activities, *ACS Appl. Mater. Interface* 5 (2013) 7079–7085.
- [17] C. Wen, H. Zhang, Q. Bo, T. Huang, Z. Lu, J. Lv, Y. Wang, Facile synthesis organic–inorganic heterojunctions of $\text{HsBO}_3/\text{g-C}_3\text{N}_4$ as efficient visible-light-driven photocatalyst for organic degradation, *Chem. Eng. J.* 270 (2015) 405–410.
- [18] F. Chang, Y. Xie, J. Zhang, J. Chen, C. Li, Construction of exfoliated $\text{g-C}_3\text{N}_4$ nanosheets- BiOCl hybrids with enhanced photocatalytic performance, *RSC Adv.* 4 (2014) 28519–28528.
- [19] K. Katsumata, R. Motoyoshi, N. Matsushita, K. Okada, Preparation of graphitic carbon nitride ($\text{g-C}_3\text{N}_4$)/ WO_3 composites and enhanced visible-light-driven photo-degradation of acetaldehyde gas, *J. Hazard. Mater.* 260 (2013) 475–482.
- [20] A. Akhundi, A. Habibiyanjeh, Graphitic carbon nitride nanosheets decorated with CuCr_2O_4 nanoparticles: novel photocatalysts with high performances in visible light degradation of water pollutants, *J. Colloid Interface Sci.* 504 (2017) 697–710.
- [21] J. Cai, Y. He, X. Wang, L. Zhang, L. Dong, Photodegradation of RhB over $\text{YVO}_4/\text{g-C}_3\text{N}_4$ composites under visible light irradiation, *RSC Adv.* 3 (2013) 20862–20868.
- [22] C. Liu, Y. Zhang, F. Dong, et al., Chlorine intercalation in graphitic carbon nitride for efficient photocatalysis, *Appl. Catal. B: Environ.* 203 (2017) 465–474.
- [23] H. Huang, K. Xiao, N. Tian, et al., Template-free precursor-surface-etching route to porous $\text{g-C}_3\text{N}_4$ thin nanosheets for enhancing photocatalytic reduction and oxidation activity, *J. Mater. Chem. A* 5 (2017) 17452–17463.
- [24] N. Tian, Y. Zhang, X. Li, K. Xiao, et al., Precursor-reforming protocol to 3D mesoporous $\text{g-C}_3\text{N}_4$ established by ultrathin self-doped nanosheets for superior hydrogen evolution, *Nano Energy* 38 (2017) 72–81.
- [25] M. Mousavi, A. Habibiyanjeh, M. Abitorabi, Fabrication of novel magnetically separable nanocomposites using graphitic carbon nitride, silver phosphate and silver chloride and their applications in photocatalytic removal of different pollutants using visible-light irradiation, *J. Colloid Interface Sci.* 480 (2016) 218–231.
- [26] M. Mousavi, A. Habibi-Yangjeh, Novel magnetically separable $\text{g-C}_3\text{N}_4/\text{Fe}_3\text{O}_4/\text{Ag}_3\text{PO}_4/\text{Co}_3\text{O}_4$ nanocomposites: visible-light-driven photocatalysts with highly enhanced activity, *Adv. Powder Technol.* 28 (2017) 1540–1553.
- [27] A. Habibi-Yangjeh, A. Akhundi, Facile preparation of novel quaternary $\text{g-C}_3\text{N}_4/\text{Fe}_3\text{O}_4/\text{AgI}/\text{Bi}_2\text{S}_3$ nanocomposites: magnetically separable visible-light-driven photocatalysts with significantly enhanced activity, *RSC Adv.* 6 (2016) 106572–106583.
- [28] A. Akhundi, A. Habibi-Yangjeh, High performance magnetically recoverable $\text{g-C}_3\text{N}_4/\text{Fe}_3\text{O}_4/\text{Ag}/\text{Ag}_2\text{SO}_3$ plasmonic photocatalyst for enhanced photocatalytic degradation of water pollutants, *Adv. Powder Technol.* 28 (2017) 565–574.
- [29] C. Miranda, H. Mansilla, J. Yáñez, S. Obregón, G. Colón, Improved photocatalytic activity of $\text{g-C}_3\text{N}_4/\text{TiO}_2$ composites prepared by a simple impregnation method, *J. Photochem. Photobiol. A: Chem.* 253 (2013) 16–21.
- [30] L.Q. Ye, J.Y. Liu, Z. Jiang, T.Y. Peng, L. Zan, Facets coupling of $\text{BiOBr-g-C}_3\text{N}_4$ composite photocatalyst for enhanced visible-light-driven photocatalytic activity, *Appl. Catal. B: Environ.* 142–143 (2013) 1–7.
- [31] N. Tian, H.W. Huang, Y.X. Guo, Y.H. Zhang, A $\text{g-C}_3\text{N}_4/\text{Bi}_2\text{O}_2\text{CO}_3$ composite with high visible-light-driven photocatalytic activity for rhodamine B degradation, *Appl. Surf. Sci.* 322 (2014) 249–254.
- [32] M. Ou, Q. Zhong, S. Zhang, L. Yu, Ultrasound assisted synthesis of heterogeneous $\text{g-C}_3\text{N}_4/\text{BiVO}_4$ composites and their visible-light-induced photocatalytic oxidation of NO in gas phase, *J. Alloy. Compd.* 626 (2015) 401–409.
- [33] Y. Peng, Z. Guo, J. Yang, D. Wang, W. Yuan, Enhanced photocatalytic H_2 evolution over micro-SiC by coupling with CdS under visible light irradiation, *J. Mater. Chem. A* 2 (2014) 6296–6300.
- [34] J.Y. Hao, Y.Y. Wang, X.L. Tong, G.Q. Jin, X.Y. Guo, Photocatalytic hydrogen production over modified SiC nanowires under visible light irradiation, *Int. J. Hydrog. Energy* 37 (2012) 15038–15044.
- [35] X.F. Zhou, Q.Z. Gao, X. Li, Y.J. Liu, S.S. Zhang, Ultra-thin SiC layer covered graphene nanosheets as advanced photocatalysts for hydrogen evolution, *J. Mater. Chem. A* 3 (2015) 10999–11005.
- [36] Y. Li, Z. Yu, J. Meng, Y. Li, Enhancing the activity of a SiC- TiO_2 composite catalyst for photo-stimulated catalytic water splitting, *Int. J. Hydrog. Energy* 38 (2013) 3898–3904.
- [37] Y.T. Gao, Y.Q. Wang, Y.X. Wang, Photocatalytic hydrogen evolution from water on SiC under visible light irradiation, *React. Kinet. Catal. Lett.* 91 (2007) 12–19.
- [38] N.A. Kouamé, D. Robert, V. Keller, P. Nguyen, Preliminary study of the use of β -SiC foam as a photocatalytic support for water treatment, *Catal. Today* 161 (2011) 3–7.
- [39] A. Fernández, G.M. Arzac, U.F. Vogot, F. Hosoglu, A. Borgschulte, Investigation of a Pt containing washcoat on SiC foam for hydrogen combustion applications, *Appl. Catal. B: Environ.* 180 (2016) 336–343.
- [40] C. Gomez-Solis, I. Juárez-Ramírez, E. Moctezuma, L.M. Torres-Martínez, Photodegradation of indigo carmine and methylene blue dyes in aqueous solution by SiC- TiO_2 catalysts prepared by sol-gel, *J. Hazard. Mater.* 217–218 (2012) 194–199.
- [41] D. Wang, W. Wang, Q. Wang, Z. Guo, W. Yuan, Spatial separation of Pt and IrO_2 catalysts on SiC surface for enhanced photocatalysis, *Mater. Lett.* 201 (2017) 114–117.
- [42] T. Zou, C. Xie, Y. Liu, S. Zhang, Z. Zou, Full mineralization of toluene by photocatalytic degradation with porous TiO_2/SiC nanocomposite film, *J. Alloy. Compd.* 552 (2013) 504–510.
- [43] M. Wang, J. Chen, X. Liao, Z. Liu, J. Zhang, Highly efficient photocatalytic hydrogen production of platinum nanoparticle-decorated SiC nanowires under simulated sunlight irradiation, *Int. J. Hydrog. Energy* 39 (2014) 14581–14587.
- [44] T.T. Li, L.H. Zhao, Y.M. He, J. Cai, M.F. Luo, J.J. Lin, Synthesis of $\text{g-C}_3\text{N}_4/\text{SmVO}_4$ composite photocatalyst with improved visible light photocatalytic activities in RhB degradation, *Appl. Catal. B: Environ.* 129 (2013) 255–263.
- [45] C. Liang, C. Liu, H. Wang, L. Wu, Z. Jiang, SiC- Fe_3O_4 dielectric–magnetic hybrid nanowires: controllable fabrication, characterization and electromagnetic wave absorption, *J. Mater. Chem. A* 2 (2014) 16397–16402.
- [46] H. Yan, Y. Chen, S. Xu, Synthesis of graphitic carbon nitride by directly heating sulfuric acid treated melamine for enhanced photocatalytic H_2 production from

- water under visible light, *Int. J. Hydrog. Energy* 37 (2012) 125–133.
- [47] F. Chang, Y. Xie, C. Li, J. Chen, J. Luo, A facile modification of g-C₃N₄ with enhanced photocatalytic activity for degradation of methylene blue, *Appl. Surf. Sci.* 280 (2013) 967–974.
- [48] B. Wang, J. Zhang, F. Huang, Enhanced visible light photocatalytic H₂ evolution of metal-free g-C₃N₄/SiC heterostructured photocatalysts, *Appl. Surf. Sci.* 391 (2017) 449–456.
- [49] Y. Zhang, T. Xia, P. Wallenmeyer, C.X. Harris, A.A. Peterson, Photocatalytic hydrogen generation from pure water using silicon carbide nanoparticles, *Energy Technol.* 2 (2014) 183–187.
- [50] F. Chang, C. Li, J. Chen, J. Wang, J. Luo, Enhanced photocatalytic performance of g-C₃N₄ nanosheets–BiOBr hybrids, *Superlattices Microstruct.* 76 (2014) 90–104.
- [51] J. Di, J. Xia, S. Yin, H. Xu, L. Xu, Preparation of sphere-like g-C₃N₄/BiOI photocatalysts via a reactable ionic liquid for visible-light-driven photocatalytic degradation of pollutants, *J. Mater. Chem. A* 2 (2014) 5340–5351.
- [52] J. Xu, L. Zhang, R. Shi, Y. Zhu, Chemical exfoliation of graphitic carbon nitride for efficient heterogeneous photocatalysis, *J. Mater. Chem. A* 1 (2013) 14766–14772.
- [53] H. Huang, X. Li, J. Wang, F. Dong, Anionic group self-doping as a promising strategy: band-gap engineering and multi-functional applications of high-performance CO₃ doped Bi₂O₂CO₃, *ACS Catal.* 5 (2015) 4094–4103.
- [54] S. Tu, H. Huang, T. Zhang, Y. Zhang, Controllable synthesis of multi-responsive ferroelectric layered perovskite-like Bi₄Ti₃O₁₂: photocatalysis and piezoelectric-catalysis and mechanism insight, *Appl. Catal. B: Environ.* 219 (2017) 550–562.
- [55] H. Huang, S. Tu, C. Zeng, Macroscopic polarization enhancement promoting photo- and piezoelectric-induced charge separation and molecular oxygen activation, *Angew. Chem. Int. Ed.* 56 (2017) 11860–11864.
- [56] L. Ye, J. Liu, C. Gong, L. Tian, T. Peng, Two different roles of metallic Ag on Ag/AgX/BiOX (X = Cl, Br) visible light photocatalysts: surface plasmon resonance and Z-scheme bridge, *ACS Catal.* 2 (2012) 1677–1683.
- [57] H. Fu, C. Pan, W. Yao, Y. Zhu, Visible-light-induced degradation of rhodamine B by nanosized Bi₂WO₆, *J. Phys. Chem. B* 109 (2005) 22432–22439.